



ELSEVIER

Available online at [www.sciencedirect.com](http://www.sciencedirect.com)

SCIENCE @ DIRECT®

Physics Letters B 578 (2004) 23–32

PHYSICS LETTERS B

[www.elsevier.com/locate/physletb](http://www.elsevier.com/locate/physletb)

## High rate production of antihydrogen

ATHENA Collaboration

M. Amoretti<sup>a</sup>, C. Amsler<sup>b</sup>, G. Bazzano<sup>c,d</sup>, G. Bonomi<sup>e</sup>, A. Bouchta<sup>e</sup>, P. Bowe<sup>f</sup>,  
C. Carraro<sup>a,g</sup>, C.L. Cesar<sup>h</sup>, M. Charlton<sup>i</sup>, M. Doser<sup>e</sup>, V. Filippini<sup>c,d</sup>, A. Fontana<sup>c,d</sup>,  
M.C. Fujiwara<sup>j,k</sup>, R. Funakoshi<sup>k</sup>, P. Genova<sup>c,d</sup>, J.S. Hangst<sup>f</sup>, R.S. Hayano<sup>k</sup>,  
L.V. Jørgensen<sup>i</sup>, V. Lagomarsino<sup>a,g</sup>, R. Landua<sup>e</sup>, D. Lindelöf<sup>b</sup>, E. Lodi Rizzini<sup>c,l</sup>,  
M. Macri<sup>a</sup>, N. Madsen<sup>f</sup>, G. Manuzio<sup>a,g</sup>, M. Marchesotti<sup>e</sup>, P. Montagna<sup>c,d</sup>, H. Pruys<sup>b</sup>,  
C. Regenfus<sup>b</sup>, P. Riedler<sup>e</sup>, A. Rotondi<sup>c,d</sup>, G. Rouleau<sup>e</sup>, G. Testera<sup>a</sup>, A. Variola<sup>a</sup>,  
D.P. van der Werf<sup>i</sup>

<sup>a</sup> *Istituto Nazionale di Fisica Nucleare, Sezione di Genova, 16146 Genova, Italy*

<sup>b</sup> *Physik-Institut, Zurich University, CH-8057 Zurich, Switzerland*

<sup>c</sup> *Istituto Nazionale di Fisica Nucleare, Università di Pavia, 27100 Pavia, Italy*

<sup>d</sup> *Dipartimento di Fisica Nucleare e Teorica, Università di Pavia, 27100 Pavia, Italy*

<sup>e</sup> *EP Division, CERN, CH-1211 Geneva 23, Switzerland*

<sup>f</sup> *Department of Physics and Astronomy, University of Aarhus, DK-8000 Aarhus C, Denmark*

<sup>g</sup> *Dipartimento di Fisica, Università di Genova, 16146 Genova, Italy*

<sup>h</sup> *Instituto de Fisica, Universidade Federal do Rio de Janeiro, Rio de Janeiro 21945-970, Brazil*

<sup>i</sup> *Department of Physics, University of Wales Swansea, Swansea SA2 8PP, UK*

<sup>j</sup> *Atomic Physics Laboratory, RIKEN, Saitama 351-0198, Japan*

<sup>k</sup> *Department of Physics, University of Tokyo, Tokyo 113-0033, Japan*

<sup>l</sup> *Dipartimento di Chimica e Fisica per l'Ingegneria e per i Materiali, Università di Brescia, 25123 Brescia, Italy*

Received 27 August 2003; accepted 14 October 2003

Editor: W.-D. Schlatter

### Abstract

We show that antihydrogen production is the dominant process when mixing antiprotons and positrons in the ATHENA apparatus, and that the initial production rate exceeds 300 Hz, decaying to 30 Hz within 10 s. A fraction of 65% of all observed annihilations is due to antihydrogen.

© 2003 Elsevier B.V. All rights reserved.

*E-mail address:* [michael.doser@cern.ch](mailto:michael.doser@cern.ch) (M. Doser).

## 1. Introduction and motivation

The initial observation of cold antihydrogen by the ATHENA experiment [1] was based on a geometrical reconstruction of the annihilation of antihydrogen atoms on an event-by-event basis, in which both antiproton and positron were detected. This was made possible by the presence of a high granularity detector for charged particle tracking and photon detection [2]. The detection efficiency for a full topological reconstruction was low ( $\sim 0.2\%$ ) due to the  $\sim 20\%$  detection efficiency for each of the two 511 keV photons from  $e^+e^-$  annihilations and stringent software cuts. Alternatively, other observables with a lower specificity to antihydrogen, but higher reconstruction efficiency, can be used to measure antihydrogen production, verify consistency and extract rates.

In this Letter, we will use a series of observables (vertex distribution, opening angle, trigger rate) together with Monte Carlo simulations of the ATHENA apparatus to determine the absolute production rate of antihydrogen in the ATHENA experiment. We will show that a dominant fraction of detector triggers come from antihydrogen annihilation, with a small contribution from antiproton-only annihilations; triggers caused by annihilation events can thus be used as a proxy for antihydrogen production, allowing a rapid exploration of the various relevant parameters influencing antihydrogen production.

## 2. Apparatus and data sets

The ATHENA apparatus [3] consists of four main subsystems: the antiproton catching trap, the mixing trap, and the antihydrogen detector, located in a 3 T superconducting solenoid and a separate positron accumulator [4], with its own 0.14 T magnet. Charged particle traps are variations of the Penning trap consisting of hollow cylindrical electrodes and a coaxial magnetic field to provide axial and radial confinement, respectively. A cryogenic ( $\sim 10$  K) heat exchanger in the bore of the superconducting magnet surrounds and cools the catching and mixing traps, and forms an ultrahigh vacuum region, which is separated from the positron accumulator by a valve.

The antihydrogen detector, of 75 (140) mm inner (outer) diameter, and 250 mm length is located inside

the magnet bore, and surrounds the heat exchanger in the region of the mixing trap (25 mm inner diameter). It consists of a charged particle tracking detector in the form of two cylindrical layers of 16 double-sided silicon strip detectors ( $160 \times 19 \text{ mm}^2$ ) each. This is surrounded by a photon detector in the form of a cylindrical array of 192 scintillating pure CsI crystals ( $17 \times 17.5 \times 13 \text{ mm}$ ) read out by avalanche photodiodes. The trajectories of charged particles through the tracking detector are reconstructed as straight lines; since only two hits are measured for each track, the curvature due to the magnetic field cannot be reconstructed. The antiproton annihilation vertex is determined by calculating the intersection between two or more tracks. The uncertainty in the vertex determination is  $\sigma = 4 \text{ mm}$ , both in the transverse plane ( $x$ - $y$  coordinates) and along the magnet axis ( $z$ -coordinate), and is dominated by the error due to the straight track approximation. The photon detector measures the energies of low energy photons (through the photoconversion peak) down to about 200 keV. It is sensitive to the  $2\gamma$  (two 511-keV photons, which are emitted back-to-back), as well as to the  $3\gamma$  modes of positron-electron annihilations. Its energy resolution is 24% (FWHM) at 511 keV. We call an energy deposit in a single crystal an ‘isolated photon’ if none of the eight neighboring crystals detect an energy deposit above threshold, if no signal is detected on the silicon strip counter directly below it and if none of the reconstructed tracks extrapolate into the crystal or its eight neighbors.

Antiprotons from the CERN antiproton decelerator (AD) and positrons from the decay of  $^{22}\text{Na}$  are accumulated in their respective catching traps, before being transferred into separate wells in the mixing trap region. After allowing the positrons to cool by synchrotron radiation to the ambient temperature of about 15 K, we form a nested [5] trap around the positron well. A mixing cycle starts when approximately  $10^4$  antiprotons are injected with a relative energy of about 15 eV into the cloud of  $7.5 \times 10^7$  positrons by pulsing the trap containing the antiprotons, and lasts 180 s. We call this type of mixing ‘cold mixing’. A second type of mixing called ‘hot mixing’ maintains the positrons at a temperature of several thousand Kelvin through radio frequency heating of their axial motion [6,7]. This effectively suppresses the two mechanisms of antihydrogen formation (radiative recombination and

three-body recombination) expected to be important in ATHENA.

Absolute comparisons between the different data sets require cross normalizations. Each mixing cycle uses antiprotons accumulated during three AD cycles. For each shot, the number of antiprotons delivered to the ATHENA experiment is determined by plastic scintillators which surround the apparatus, and are capable of integrating the intense burst of secondary particles produced by antiprotons annihilating in the beam degrader at the entrance of the antiproton catching trap [8]. These detectors determine the number of trapped antiprotons and antiprotons injected into the positron cloud for each mixing cycle. Antiproton losses are continuously monitored by a further set of scintillators. The number of antiprotons remaining at the end of a cycle is determined by annihilating them in a short burst, and counting the annihilation products using the same scintillators [9]. Positron plasma characteristics (e.g., density and aspect ratio) are monitored during mixing through nondestructive detection of plasma axial modes [6,7]. Event triggers, consisting of at least three hits on either side of the outer silicon strip detectors, initiate readout of both silicon and CsI modules. With the exception of during the read-out (dead time of 300  $\mu$ s per event), the trigger rate is continuously recorded, as are the readout dead times. Trigger rates in this Letter are given for a standard mixing cycle, which uses  $10^4$  antiprotons.

### 3. Monte Carlo simulation

The ATHENA apparatus simulation [3] is based on Geant 3.21 [10] and was used to study the detection efficiency for antiproton annihilations, positron annihilations and antihydrogen annihilations, and to determine the background signals. The Monte Carlo contains a description of the ATHENA apparatus (electrodes, vacuum tubes, cabling, detectors, superconducting magnet), and describes the physical processes of antiproton–proton and positron–electron annihilation. In the latter case, the relative contribution of the  $2\gamma$ - to the  $3\gamma$ -mode must be experimentally determined, and will be discussed below. Simulated antihydrogen annihilations assume isotropically distributed, spatially and temporally coincident antiproton–proton and positron–electron (to  $2\gamma$ ) annihilations.

In the original publication [1] on antihydrogen production, we conservatively assumed that all detectors were fully efficient; the present simulation now accounts for inefficiencies and module-to-module variations in resolution, and introduces detector noise at the experimentally measured rate.

Data sets of pure antiproton or positron annihilations on the Penning trap electrodes are used to study a number of observables (charged particle multiplicity, photon multiplicity, photon energy distribution, vertex distribution), to verify that the Monte Carlo correctly describes the ATHENA detector and the underlying physics [3]. These data sets are obtained by modifying the shape of the trapping wells, inducing a slow radial outward transport of the trapped particles. They eventually reach the well-shaping electrodes where they annihilate. We observe that these annihilations are enhanced at the junction between electrodes and localized in  $\phi$  (the azimuthal coordinate around the central axis of the apparatus) [11], possibly due to small local mechanical imperfections and field misalignments.

Fig. 1 shows a comparison between Monte Carlo simulations and real data. For antiproton annihilations on the trap electrodes, Fig. 1(a) shows the reconstructed radial vertex distribution. The simulation is in good agreement with the experimental distribution. Fig. 1(b) shows the measured single isolated photon energy distribution for ‘cold mixing’ and antiproton annihilations on the trap electrodes. A comparison with the same distributions for the Monte Carlo (Fig. 1(c)) shows that here, too, the simulated and experimental distributions are in good agreement. In addition, Fig. 1(b) and (c) underline the fact that the 511 keV peak is absent in pure antiproton annihilations, and is associated exclusively with  $e^+$  annihilations.

### 4. Vertex distributions

The analysis of the data will be presented as follows: in a first step, the vertex distributions are analyzed to determine the relative rates of the contributing components (antihydrogen and antiproton-only annihilations). In a second step, this decomposition is combined with Monte Carlo efficiencies and compared with measured  $2\gamma$  opening angles (for completely reconstructed events with vertex and two 511 keV  $\gamma$ 's)

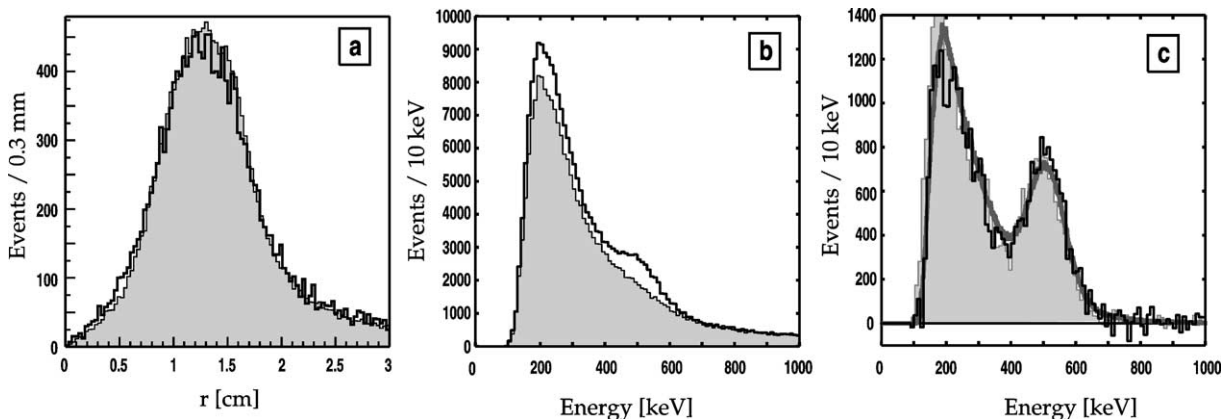


Fig. 1. (a) Reconstructed radial vertex distribution (bold line: data; shaded area: Monte Carlo).  $r = 0$  corresponds to the central axis of the apparatus,  $r = 1.25$  cm to the position of the electrodes; (b) energy distribution for isolated photons during ‘cold mixing’ (bold line) and for antiproton annihilations on the trap electrodes (shaded area) for the same number of vertices. The contribution of noise lies below 100 keV, and has been suppressed by software cuts. The peak at 511 keV (total absorption) and the rise below 400 keV (Compton scattering) stem from  $e^+e^- \rightarrow 2\gamma$  annihilations; (c) difference between the two distributions of (b) (bold line). The broad grey line corresponds to pure  $e^+$  annihilations from a dedicated experiment using only positrons (rescaled), the shaded area to the difference between Monte Carlo simulations of the two processes in (b).

to confirm these assignments. Finally, the temporal evolution of the two components are investigated, and compared with the detector trigger rates. All data are corrected for detector read-out dead time based on the trigger rate at the time of read out and the experimentally determined average dead time for that trigger rate.

Two main processes are expected to contribute to the data measured with the ATHENA apparatus: (1) antiproton annihilation on positive ions trapped together with the positrons or on rest gas, and (2) antihydrogen annihilation on the electrode surface. Here, we use two data sets which consist (in different proportions) of the two processes: a ‘cold mixing’ data set (338 500 events with reconstructed vertices) and a ‘hot mixing’ data set (33 870 events with reconstructed vertices). In Ref. [1], we have shown that antihydrogen production is observed in the ‘cold mixing’ data, and is strongly suppressed in the ‘hot mixing’ data.

To study the vertex distributions for the different data sets, we define a fiducial region ( $z \in [-0.5, 1.5]$  cm) centered on the positron plasma. The length of the fiducial region is chosen so as to minimize the number of electrode junctions where the aforementioned localized losses could take place. The systematic error on the results of the following fits includes the effect of varying this length. The radial ( $r$ ) vertex

distributions ( $dN/dr$ ) in this fiducial region for ‘hot mixing’ ( $N = 10620$  events, Fig. 2(a)) and for ‘cold mixing’ ( $N = 133700$  events, Fig. 2(c)) show a notable difference. In the case of ‘hot mixing’, we observe an enhancement at small radii, while in the case of ‘cold mixing’, the enhancement is consistent with the radius of the trap electrodes (1.25 cm), but with some additional signal at smaller radii. Fig. 2(b) shows the radial vertex distribution for antiprotons intentionally annihilated on the trap electrodes of the mixing trap (5 889 events). These events have the same radial vertex distribution as antihydrogen annihilations.

We now fit the measured radial vertex distribution of the ‘cold mixing’ data (Fig. 2(c)) as a linear superposition of the radial vertex distributions for antiproton annihilations on the trap electrodes (Fig. 2(b)) and of the ‘hot mixing’ data (Fig. 2(a)). The result of the fit is superimposed on the data in Fig. 2(c). The fit describes ‘cold mixing’ data as consisting to  $(69 \pm 1)\%$  of annihilations on the trap electrodes ( $92434 \pm 434$  events) and to  $(31 \pm 1)\%$  of (centrally enhanced) annihilations from ‘hot mixing’ ( $40622 \pm 563$  events).

This result is in agreement with a 2-dimensional fit to the  $x$ - $y$  vertex distribution for ‘cold mixing’ (Fig. 3(a)) as the weighted sum of the  $x$ - $y$  distributions for ‘hot mixing’ and for Monte Carlo simulated antihydrogen atoms (uniformly generated from  $r = 0$

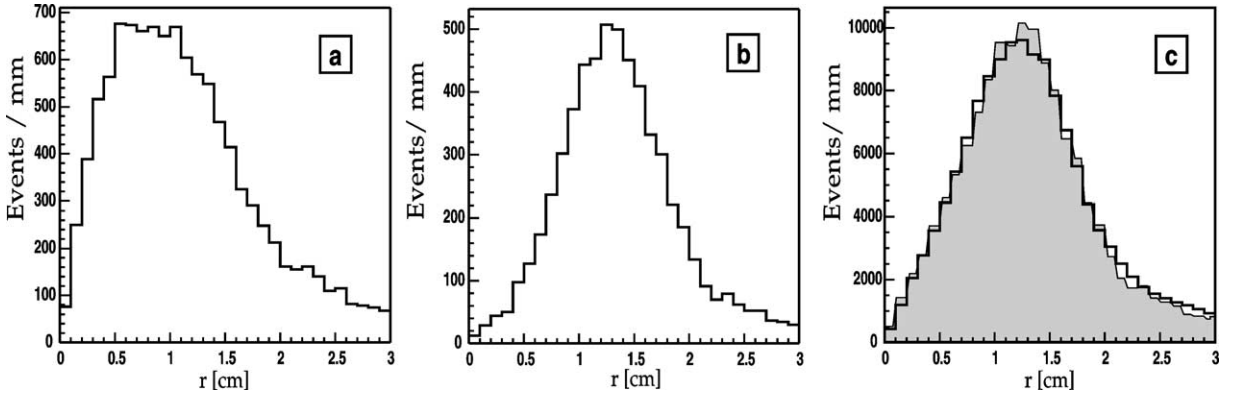


Fig. 2. (a) Radial vertex distribution for ‘hot mixing’ ( $z \in [-0.5, 1.5]$  cm); (b) radial vertex distribution for antiproton annihilations on the trap electrodes; (c) radial vertex distribution for ‘cold mixing’ ( $z \in [-0.5, 1.5]$  cm). The bold line is the result of the fit described in the text.

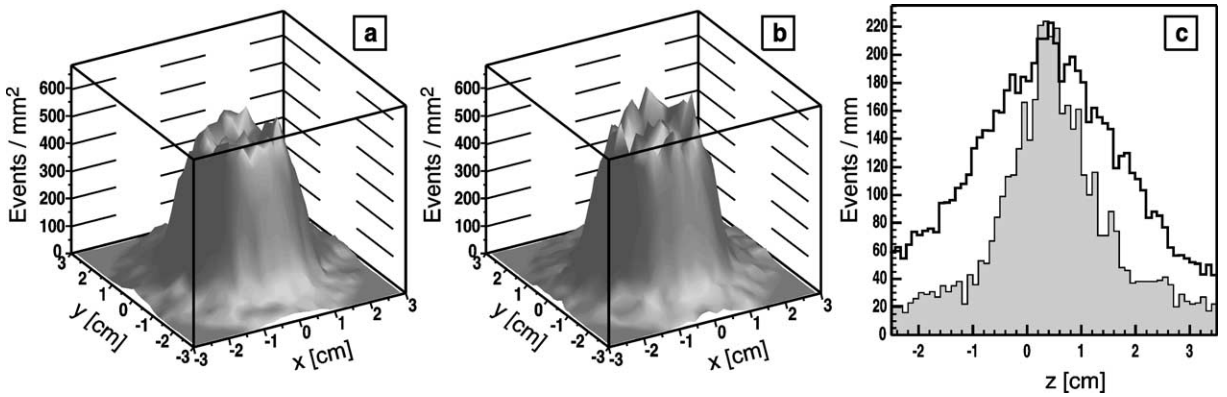


Fig. 3. (a)  $x$ - $y$  distribution of the reconstructed vertices in the fiducial volume for ‘cold mixing’; (b) result of the fit described in the text; (c)  $z$ -distribution of central annihilations ( $r < 0.5$  cm) for ‘hot mixing’ (shaded area). The solid line corresponds to the  $z$ -distribution of annihilations on the trap electrode wall ( $r \in [0.75, 1.75]$  cm) for ‘cold mixing’, and has been rescaled by a factor of 0.044 for comparison. The two  $r$ -windows are chosen in accordance with the vertex resolution of 4 mm.

and  $|z| < 1.5$  cm and isotropically emitted) annihilating on the trap electrode walls. Fig. 3(b) shows the result of the fit, which gives an antihydrogen contribution of  $(64 \pm 3)\%$ .

Two components thus account for the ‘cold mixing’ vertex distribution. The main component corresponds to annihilations on the trap electrodes, and is characterized by an isotropic distribution on the inner surface of the electrodes around the trap axis (Fig. 3(a)), and a broad distribution along the  $z$ -axis (Fig. 3(c)), as expected for antihydrogen annihilations. The second component is centered on the axis of the trap. Its longitudinal extent (Fig. 3(c)) of  $\sim 2$  cm is incompatible with a point source (since the  $z$ -vertex resolution is 4 mm), but is close to the 3 cm length of the positron

plasma. These events are compatible with being antiproton annihilations on positive ions trapped in the central region of the positron well (or possibly on rest gas).

## 5. $2\gamma$ opening angles

Having determined the ratio of the two components (annihilations on the electrodes and annihilations close to the trap axis), we now use the photon information to investigate their nature. For ‘cold mixing’ events with a vertex in the fiducial region, we select the sub-sample containing two isolated photons with energies in an energy window of  $2.5\sigma$  around

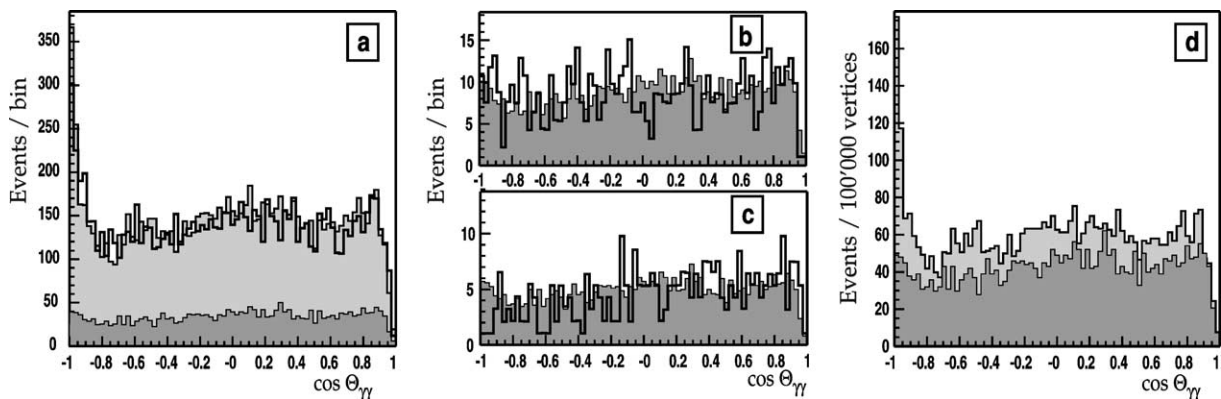


Fig. 4. (a)  $\cos\theta_{\gamma\gamma}$  distribution for ‘cold mixing’ data (bold line, 10410 events). The light shaded area is the prediction from the fit to the radial vertex distribution. The dark shaded distribution is that of the ‘hot mixing’ contribution in the same fit; (b)  $\cos\theta_{\gamma\gamma}$  distribution for ‘hot mixing’ data (bold line: data; shaded area: Monte Carlo prediction based on the number of vertices in the ‘hot mixing’ data set); (c)  $\cos\theta_{\gamma\gamma}$  distribution for antiproton annihilations on the trap electrodes (bold line: data; shaded area: Monte Carlo prediction); (d) Monte Carlo  $\cos\theta_{\gamma\gamma}$  distribution for antihydrogen annihilations on the trap electrodes (light distribution) and for antiproton annihilations at the center of the apparatus (dark distribution). Both distributions correspond to the same number of 100 000 reconstructed vertices.

511 keV (‘complete’ events). For each event in the selected sub-sample, we determine the  $2\gamma$  opening angle  $\theta_{\gamma\gamma}$  as subtended from the reconstructed annihilation vertex to the geometric centers of the hit crystals. For antihydrogen events, assuming  $e^+e^-$  annihilations to  $2\gamma$  only,  $\cos\theta_{\gamma\gamma}$  should be  $-1$ . However, due to additional bremsstrahlung photons falling in the 511 keV energy window, and the low detection efficiency for 511 keV photons, this topology is quite rare. Indeed, a large fraction of antihydrogen events exhibit a random angle between two isolated photons falling in our 511 keV energy window (Fig. 4(d), pure antihydrogen Monte Carlo). Fig. 4(a) shows the  $\cos\theta_{\gamma\gamma}$  distribution for ‘cold mixing’, Fig. 4(b) the distribution for ‘hot mixing’ and Fig. 4(c) for antiproton annihilations on the trap electrodes. The peak at  $-1$  in Fig. 4(a) (which is absent in both Fig. 4(b) and (c)) is caused by antihydrogen annihilation.

We generate Monte Carlo events for the two components of the fit to the radial vertex distribution. The first component consists of antihydrogen annihilations on the trap electrodes, for which the  $\cos\theta_{\gamma\gamma}$  distribution corresponds to the light distribution in Fig. 4(d). The second component consists of antiproton annihilations at the center of the apparatus (Fig. 4(d), dark distribution). Note that neither the shape, nor the amplitude, of the distribution changes if instead, we simulate antiproton annihilations on the trap electrodes.

Furthermore, this simulation of antiprotons annihilating on the electrodes is in good agreement with the experimentally obtained  $\cos\theta_{\gamma\gamma}$  distribution for antiprotons intentionally annihilated on the trap electrodes (Fig. 4(c), trap electrode annihilation data set). The two components are normalized to the 92 434 events with vertices on the trap-electrodes, and 40 622 events with central vertices from the radial vertex fit. The  $\cos\theta_{\gamma\gamma}$  distribution for these two Monte Carlo data sets are added together without any renormalization, and are superimposed on the experimental distribution of Fig. 4(a). The prediction based on the radial vertex fit together with the simulations is in good agreement with the data. This is a good indication that the assumptions that the annihilations on the trap electrodes correspond to antihydrogen events, while the central annihilations correspond to antiproton-only annihilations, are correct, and that consequently, around 2/3 of the events in the fiducial volume stem from antihydrogen annihilation. A fit of the distribution of Fig. 4(a) as a linear superposition of the two distributions of Fig. 4(d), using a fitting technique adapted to finite Monte Carlo samples [12], can be used as an independent determination of the fraction of antihydrogen. The resulting value of  $(60 \pm 5)\%$  is in good agreement with the values from the fits of the vertex distribution.

This conclusion is corroborated by comparing the fraction of ‘complete’ events in the different data sets.

Table 1

Summary of the statistics of the different data sets used in this analysis: number of events with a vertex, number of events with a vertex and two isolated 511 keV photons ('complete events'), and the fraction of complete events

Data set	Number of events	Events with $2\gamma$	Fraction of complete events (%)
Cold mixing	133 700	10 400	$7.79 \pm 0.08$
Hot mixing	10 620	643	$6.06 \pm 0.25$
Antiproton annihilation	5 889	339	$5.8 \pm 0.3$
Antihydrogen (Monte Carlo)	143 118	12 798	$8.94 \pm 0.08$
Antiproton annihilation (Monte Carlo)	142 415	8 429	$5.92 \pm 0.06$

Table 1 summarizes the results for 'cold mixing', 'hot mixing', and pure antiproton annihilations, as well as for Monte Carlo simulations of antihydrogen annihilations on the trap electrodes, and of antiproton annihilations at the center of the traps (300 000 events generated for each). From these numbers, it is apparent that the fraction of 'complete' events in 'hot mixing' and antiproton annihilations on the trap electrodes are compatible with the Monte Carlo prediction for pure antiproton annihilation. On the other hand, the fraction in the 'cold mixing' data is intermediate to pure antihydrogen production and antiproton annihilations. The fraction of antihydrogen events in 'cold mixing' extracted from these numbers by linear interpolation (between the Monte Carlo values for antihydrogen and antiproton-only annihilations) of  $(62 \pm 3)\%$  is in good agreement with the values from the vertex fits. The uncertainties are of statistical nature.

In summary, several methods relying on different observables with different systematic uncertainties produce consistent estimates that  $(65 \pm 5)\%$  of all vertices of a 'cold mixing' cycle are due to antihydrogen annihilation, where the (systematic) error covers the variations between the different methods used and small variations in the length of the fiducial volume.

## 6. Time evolution and trigger rates

Next we study the temporal evolution of the 'cold mixing' data, by investigating the radial vertex distribution as a function of time from the moment antiprotons are injected into the positrons. For each time slice, the radial vertex distribution for events in the fiducial volume is fit to the same measured components as in Section 4: annihilations on the trap electrodes (shown to stem from antihydrogen annihilations in Section 5),

and 'hot mixing' data. The result of the vertex fit in the different time slices is shown in Fig. 5(a). A noteworthy feature of the fits is that the time evolution of the two components is different, the antihydrogen component accounting for over 85% of the vertices shortly after the beginning of mixing, with a slow decrease to around 50% thereafter.

Fig. 5(b) shows the time evolution of the trigger rate from the start of 'cold mixing', for the standard mixing conditions of  $10^4$  antiprotons and  $7.5 \times 10^7$  positrons. This distribution is characterized by a high initial value and a slow decay (with a time scale of several seconds). We compare this distribution with the time evolution of all events with reconstructed vertices by correcting the latter for detection efficiency. Two terms enter this correction: the probability for a triggered event to have a reconstructed vertex ( $(52 \pm 2)\%$ , as determined both from Monte Carlo and real data); and the correction for vertices lying outside of the fiducial volume, but within the central volume ( $|z| < 4$  cm), of the detector ( $(50 \pm 3)\%$ , as determined from the data). After these corrections, the time evolution of the events with reconstructed vertices (Fig. 5(b) and (c), lightly shaded areas) is in reasonable agreement with that of the trigger rate. The slight discrepancy is consistent with neglecting vertices (due to, i.e., antiproton losses at the end of the nested trap) which lie outside of the central volume of the detector ( $|z| > 4$  cm), but contribute to the trigger rate. The reasonable agreement between the two distributions is an indication that the Monte Carlo determination of detection efficiencies is correct, and that the temporal decomposition of the vertex distributions can be transferred to the temporal behavior of the trigger rate.

The difference between 'cold mixing' trigger rates and 'hot mixing' trigger rates is thus due to antihydrogen production. Fig. 5(c) shows the trigger

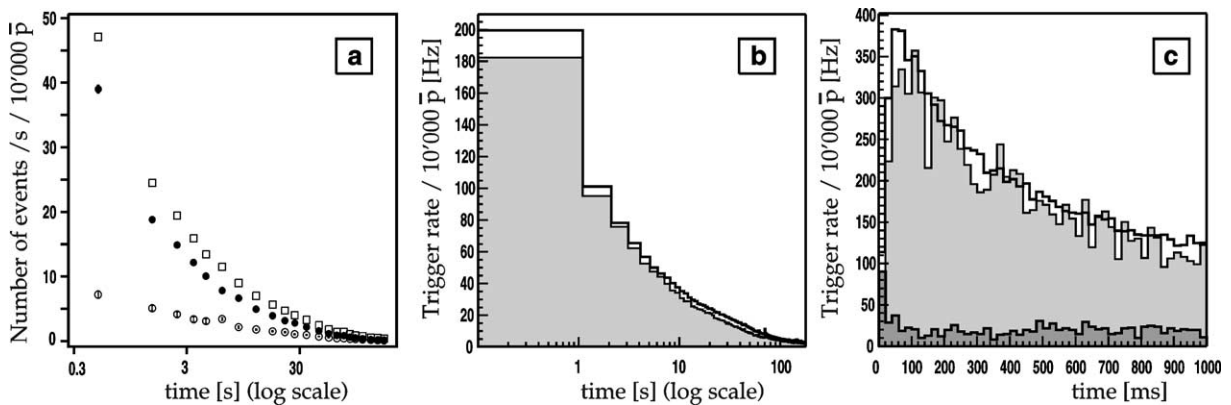


Fig. 5. (a) Time evolution of events with reconstructed vertices (fiducial volume) for ‘cold mixing’ data. The empty squares are the data, the full circles the contribution from antihydrogen annihilation, the empty circles the background (‘hot mixing’) component; (b) time evolution of all triggers (full line) and of the detection efficiency-corrected events with reconstructed vertices (light shaded area) for ‘cold mixing’; (c) the first second of the same distributions; the dark shaded area is the trigger rate for ‘hot mixing’.

rates for ‘cold mixing’ (bold line) and ‘hot mixing’ (dark shaded area), which are identified with the non-antihydrogen (background) contribution by the vertex fit. The instantaneous trigger rate for ‘cold mixing’ shortly after antiproton injection (Fig. 5(c)) thus stems dominantly from antihydrogen production with a rate exceeding 300 Hz per  $10^4$  injected antiprotons, corresponding to an antihydrogen fraction of more than 85%.

## 7. $2\gamma$ and $3\gamma$ decays

A dedicated measurement with positrons only was performed to determine the relative rates of the  $2\gamma$ - and  $3\gamma$ -modes of  $e^+e^-$  annihilations for antihydrogen atoms interacting with the electrode surfaces. This ratio influences the determination of the absolute antihydrogen production rate since only the  $2\gamma$  decay mode was used to detect antihydrogen in [1] and in this work. The ratio depends on the fraction of positrons that form positronium on the trap electrode surface [13], which is unknown.

The well holding positrons was modified in such a manner that the radial outward transport of positrons onto the trap electrodes was strongly enhanced. The photons produced in positron annihilations at the surface of the electrodes were detected in the photon detector. The trigger condition required detection of at least two photons with an energy greater than 150 keV

each. For this analysis, the isolation criterion was dropped, since no charged particles are involved.

For all events, the  $\gamma$ -multiplicity is associated with the number of photons. For events containing two or three  $\gamma$ 's, both the total energy  $E_{\text{tot}}$  and the total momentum  $P_{\text{tot}}$  (calculated from the center of the apparatus) are determined. Fig. 6(a) shows a clear signal for  $2\gamma$  events at  $E_{\text{tot}} = 2m_e c^2$  and  $P_{\text{tot}} < 200$  keV/c. The accumulation of events at  $P_{\text{tot}} = E_{\text{tot}}$  stems from  $2\gamma$  events in which one  $\gamma$  escaped detection, while the other  $\gamma$  underwent Compton scattering in a first crystal, before being detected in a second crystal. This process accounts for most detected  $3\gamma$  events, which stem from  $2\gamma$  events, where one photon is Compton scattered in a first and detected in a second crystal, while the other photon is detected in a third crystal. Fig. 6(c) shows a distribution for  $3\gamma$  events satisfying  $|E_{\text{tot}} - 2m_e c^2| < 200$  keV, where the total momentum of the three photons is plotted versus the smallest of the three angles between any two detected photons (determined from the center of the apparatus). Compton scattered photons are expected to accumulate at small minimum angle ( $\cos \theta_{\text{min}} \sim 1$ ), while the box indicates the expected signal region around  $P_{\text{tot}} \sim 0$  corresponding to  $e^+e^- \rightarrow 3\gamma$ . The detection probabilities for the two decay modes are evaluated by Monte Carlo: the detection probability for the  $2\gamma$  mode (two 511 keV photons with  $\cos \theta_{\gamma\gamma} < -0.96$ ) is 1.8%. The detection probability for the  $3\gamma$  mode (three photons with  $P_{\text{tot}} < 200$  keV/c and

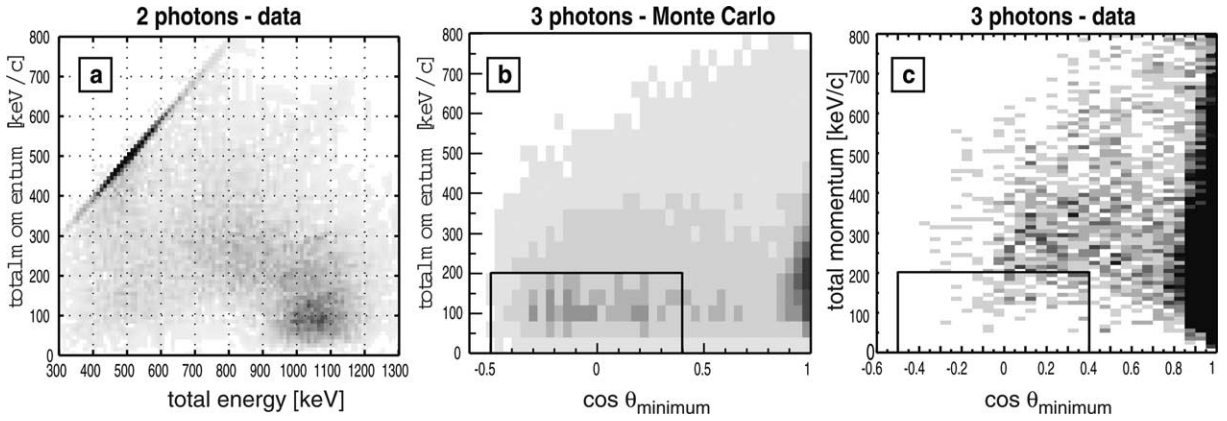


Fig. 6. (a)  $E_{\text{tot}}$  vs.  $P_{\text{tot}}$  for events containing two photons. Fully detected  $2\gamma$  events cluster at  $E_{\text{tot}} \sim 1.02$  MeV and  $P_{\text{tot}} < 200$  keV/c. (b)  $P_{\text{tot}}$  vs. the cosine of the smallest opening angle between any two  $\gamma$ 's as seen from the center of the apparatus for Monte Carlo  $3\gamma$  events. The box indicates the used signal region. (c) Same distribution for real data. The box indicates the used signal region.

$-0.5 < \cos\theta_{\min} < 0.4$ ) is 0.6%. From the observed number of 10 200  $2\gamma$  events and of 207 events in the  $3\gamma$  signal region, we conclude that  $2\gamma$  events account for at least 95% of all  $e^+e^-$  annihilations.

Assuming the same ratio of  $2\gamma$  to  $3\gamma$  decays for positrons only, and for positrons from antihydrogen atoms annihilating on the same electrode surfaces, we can thus determine that the  $3\gamma$  contribution to our antihydrogen signal does not exceed 5%, which is in agreement with the fact that we are able to consistently account for all distributions in this Letter assuming  $2\gamma$  decays only.

## 8. Discussion

The consistency that we have established between the  $\cos\theta_{\gamma\gamma}$  distribution and the trigger rates relies on assigning the  $\cos\theta_{\gamma\gamma} = -1$  signal to antihydrogen. We have investigated all conceivable sources, which might mimic this topology, to ensure that this assignment was correct. The largest potential background (511 keV photons stemming from electromagnetic showers produced close to pure antiproton annihilations on trap electrodes, rest gas or ions) has been excluded by the absence of a peak at  $\cos\theta_{\gamma\gamma} = -1$  (Fig. 4(b) and (c)) as well as the absence of a 511 keV peak in Fig. 1(b) for pure antiproton annihilations. This can be understood by a detailed Monte Carlo study of the interaction of photons from the decay of neutral pions produced in antiproton–proton

annihilations in the electrodes (3.25 mm Au-coated Al). The consequence of the momentum transfer from these high-energy photons to the particles in the (infrequently occurring) electromagnetic showers is that they are ejected from the immediate vicinity of the annihilation vertex. Consequently, only a very small fraction (0.65%) of antiproton annihilations satisfies the selection criteria that every antihydrogen annihilation meets: that a positron annihilates in the immediate vicinity of the antiproton annihilation vertex.

We have also investigated whether simultaneous, but uncorrelated, antiproton and positron annihilations could lead to the  $\cos\theta_{\gamma\gamma} = -1$  signal. In a Monte Carlo simulation, antiproton and positron annihilations are independently generated on an event-by-event basis according to an isotropic distribution in  $\phi$ , and according to the experimental distribution along the magnet axis. With respect to the resulting  $\cos\theta_{\gamma\gamma}$  distribution, the statistical significance of the excess of the measured ‘cold mixing’ peak at  $\cos\theta_{\gamma\gamma} = -1$  over this simulated distribution (scaled to the  $\cos\theta_{\gamma\gamma} > 0$  region) is  $5.3\sigma$ , thus excluding this hypothesis as well. Furthermore, antiproton and positron loss rates (both  $< 100$  Hz) and the detector trigger time window of  $2\ \mu\text{s}$  can be used to estimate that random coincidences can contribute at most 0.1 Hz to the trigger rate. Finally, we have verified that the positron plasma is not disrupted by the antiprotons by continuously measuring the plasma modes before, during and after injection of the antiprotons.

## 9. Conclusion

We have found that antihydrogen formation is indicated by many clear and consistent signals from our detector:

- (a) a fraction of  $(65 \pm 5)\%$  of uniformly distributed annihilation vertices on the trap electrodes;
- (b) an increase in the probability that an annihilation vertex is accompanied by two photons (not necessarily back-to-back) in the 511 keV window from  $(6.06 \pm 0.25)\%$  for ‘hot mixing’ to  $(8.94 \pm 0.08)\%$  for ‘cold mixing’;
- (c) an increase in the trigger rate at the start of mixing from 20 Hz for ‘hot mixing’ to 350 Hz for ‘cold mixing’ (for  $10^4$  antiprotons and  $7.5 \times 10^7 e^4$ );
- (d) a clear peak for  $\cos\theta_{\gamma\gamma} \sim -1$  in the  $2\gamma$  opening angle distribution, for which no other explanation than antihydrogen production is possible;
- (e) a pure  $e^+e^-$  annihilation signal (a peak at 511 keV in the photon energy spectrum) in the ‘cold mixing’ data set, which is absent in the antiproton-only annihilation data set.

These results do not depend on assuming that ‘hot mixing’ represents a good approximation to the background in ‘cold mixing’; the fits to the vertex distributions (which assume this background) give compatible results to the fits to the photon distributions (which use pure antiproton annihilations as background). Furthermore, we have shown that the precise spatial distribution of the background is not critical for any of the latter fits.

We have thus determined that the observed trigger rate during ‘cold mixing’ is due to two sources. Antihydrogen production comprises over 85% of the triggers at the beginning of mixing, and declines with a time constant of several seconds. Antiproton annihilation on positive ions or on rest gas (with a slowly decreasing rate) comprises the remainder of the triggers (15% at the beginning of mixing). Integrated over a full mixing cycle of 180 s, antihydrogen production accounts for  $(65 \pm 5)\%$  of the trigger rate, which can thus be used as a proxy for fully reconstructed events.

This result, combined with the total number of triggers, the probability for an annihilation to produce a trigger ( $(86 \pm 10)\%$ , as determined from Monte Carlo and data) and the total number of antiprotons detected at the end of a mixing cycle, allows us to conclude that in 341 ‘cold mixing’ cycles in which  $2.924 \times 10^6$  antiprotons have been injected in the mixing trap, about 494 000 antihydrogen atoms have been produced. This is equivalent to an antihydrogen production efficiency of  $(17 \pm 2)\%$ .

## Acknowledgements

We gratefully acknowledge the technical contributions by J. Rochet. This work was supported by the following agencies: Istituto Nazionale di Fisica Nucleare (Italy), Conselho Nacional de Pesquisa e Desenvolvimento (CNPq), Fundação de Amparo a Pesquisa de Estado do Rio de Janeiro (FAPERJ) e Fundação CCMN/UFRJ (Brazil), Grant-in-Aid for Creative Basic Research of Monbukagakusho (Japan), the Swiss National Science Foundation, the Danish National Science Research Council, the UK Engineering and Physical Sciences Research Council.

## References

- [1] M. Amoretti, et al., Nature 419 (2002) 456.
- [2] C. Regenfus, Nucl. Instrum. Methods A 501 (2003) 65.
- [3] M. Amoretti, et al., CERN preprint CERN-EP/2003-95, Nucl. Instrum. Methods, in press.
- [4] D.P. van der Werf, et al., Appl. Surf. Sci. 194 (2002) 312.
- [5] G. Gabrielse, S. Rolston, L. Haarsma, W. Kells, Phys. Lett. A 129 (1988) 38.
- [6] M. Amoretti, et al., Phys. Rev. Lett. 91 (2003) 055001.
- [7] M. Amoretti, et al., Phys. Plasmas 10 (2003) 3056.
- [8] M.C. Fujiwara, M. Marchesotti, Nucl. Instrum. Methods A 484 (2002) 162.
- [9] M.C. Fujiwara, et al., Hyperfine Interact. 138 (2001) 153.
- [10] CERN Application Software Group, GEANT: Detector Description and Simulation Tool, CERN Program Library W5013, Geneva, 1993.
- [11] M. Amoretti, et al., Phys. Rev. Lett., submitted for publication.
- [12] R. Barlow, C. Beeston, Comput. Phys. Commun. 77 (1993) 219.
- [13] P. Schulz, K. Lynn, Rev. Mod. Phys. 60 (3) (1988) 701.